SAND2008-5303C

Constitutive Properties of Dissimilar Metal Laser Welds

C. V. Robino and B. L. Boyce
Sandia National Laboratories, Albuquerque, New Mexico USA

Abstract

Digital image correlation (DIC) methods have been developed and used to determine the constitutive tensile stress-strain response in laser welds between PH13-8 Mo and 304L stainless steels. Both continuous-wave (CW) and pulsed laser welds were examined. Testing was conducted in the transverse (cross-weld) orientation and samples were ground smooth to eliminate geometric effects (weld root notch) and lightly bead blasted to provide image speckling. The DIC method provided quantitative 2-dimensional strain maps of the deformation field throughout tensile testing, and local stress-strain response was extracted from various weld regions. As expected, steep strain gradients were observed in the test welds, but constitutive relationships could nevertheless be extracted from the important weld zones. Metallographic analysis, electron backscattered analysis, and hardness testing were used to further quantify the microstructure and its relationship to the constitutive properties. Mixing in the CW weld appeared to be less complete than in the pulsed weld, and the CW weld likely contained both martensitic and ferritic regions as well as austenite, while the pulsed weld appeared to be predominantly ferritic with some residual austenite. Although additional refinement of the technique is needed to fully characterize the differences between these CW and pulsed welds, DIC has been shown to be a powerful technique for assessing the mechanical behavior of dissimilar metal laser welds.

Introduction

The mechanical performance of welded components is closely linked to the material properties in the fusion zone and/or heat-affected zone of the weldment. To assess performance, such as by finite element methods, requires an accurate description of the constitutive stress-strain response in the weldment material. The properties in the fusion and heat-affected zone are, however, not generally easy to quantify. For large-scale welds, such as those produced by shielded metal arc welding, conventional [1, 2], subsize [3] or miniature [4] tensile bars can be extracted directly from the weld metal for subsequent tensile testing. This provides the most direct method for measuring the mechanical properties of the weld material, but requires sufficiently large weldments, and assumes homogeneous material properties across the dimensions of the tensile bar. Alternatively, welded coupons of various geometries can be tested mechanically in one or more loading conditions to assess the mechanical performance. These tests sometimes provide an empirical, non-universal description of load-displacement and failure response without providing any fundamental constitutive understanding, especially in the case of cross-weld tensile tests which sample the base metal, heat-affected zone, and fusion zone simultaneously. These complex tests can be analyzed with finite element analysis in an attempt to reverse engineer the material properties overall load-displacement response of the test structure [5-7]. However, this approach relies on assumptions to describe the bounds of material variability, and can often result in non-unique solutions.

Digital image correlation (DIC) has become widely utilized for non-contact spatially-resolved strain mapping and has been applied to a wide range of problems in mechanical behavior of materials. Some examples include the measurement of strains associated with the hole drilling method for residual stress determination [8] and assessment of inhomogeneous strain fields in forming studies [9]. In addition, the DIC technique has been used in the field of joining to determine the mechanical behavior of friction stir welds in aluminum alloys [10-14]. These studies on welded material interrogated relatively large weldments, with weld nuggets several millimeters in diameter and demonstrated the utility of the DIC method to extract the local material properties from different regions in the weldment. Recently, DIC was used to track inhomogeneous strains in miniature tensile samples taken from spot welds [4] and has been used to determine constitutive properties in laser welds in stainless steels [15] and aluminum alloys [16]. In the present study, DIC method is further extended and used to extract the local constitutive response in dissimilar metal laser welds between PH 13-8 Mo and 304L stainless steels. Both continuous wave and pulsed seam welds are considered.

Experimental Procedures

The base materials used in this study were 0.063 in. (1.6 mm) thick AISI 304L stainless steel sheet with a composition (wt%) of 0.024 C, 0.45 Si, 1.83 Mn, 0.030 P, 0.001 S, 18.2 Cr, 8.3 Ni, 0.041 N, 0.42 Cu, 0.16 Mo, bal Fe. The PH 13-8 Mo stainless steel had a composition of 0.030 C, 0.050 Si, 0.030 Mn, 0.006 P, 0.0004 S, 12.47 Cr, 8.31 Ni, 0.0018 N, 2.21 Mo, 0.980 Al, bal Fe. 0.063 in. (1.6 mm) thick sheets of PH 13-8 Mo were removed from bar stock by electrodischarge machining and surface grinding. Pairs of 1.9×3.9 in. (50×100 mm) plates with a thickness of 0.063 in. (1.6 mm) were joined along their long axis to produce 3.9×3.9 in. (100×100 mm) plates with a single laser butt weld. The 304L was welded in the fully mill annealed condition, and the PH 13-8 Mo was in the aged (H950 or H1100) condition.

Two different welding techniques were evaluated in this study: autogenous continuous wave (CW) Nd:YAG and autogenous overlapping pulsed Nd:YAG. In both cases, linear butt welds parallel to the 304L plate rolling and 13-8 bar rolling direction were produced with a Rofin CW 015 HQ Nd:YAG laser welder with fiber optic beam delivery and a maximum power rating of 1600W. The CW welds were produced using a power setting of 195W and a travel speed of 60 in/min (25.4 mm/sec); and the pulsed welds (PW) were produced using an average power setting of 45W, a pulse frequency of 20 Hz, and a travel speed of 9 in/min (3.8 mm/sec), resulting in an spot-to-spot overlap of approximately 75-80%. Both procedures resulted in partial-penetration butt welds with a nominal penetration depth of 0.020 in. (500 μm) in the 0.063 in. (1.6 mm-thick) plate. For both weldments, the plates were butted together top produce a minimum joint gap. No post-weld heat treatment was applied.

Transverse tensile samples 3.9×0.25×0.063 in. (100×6.35×1.6 mm) were extracted by electrodischarge machining from the 3.9×3.9 in. (100×100 mm) welded plate. The tensile axis of the test samples was oriented orthogonal to both the welding direction and the penetration direction as shown in Fig. 1. The partial-penetration welds resulted in an unwelded ligament in the gap between the two parent plates that would act as a notch if the bar was loaded in far-field tension, resulting in non-uniform stress and strain fields. To mitigate this effect, the unwelded ligament was removed by lapping away 0.043 in. (1.1 mm) from the back side of the weld, thereby creating a geometrically simple rectangular bar for tensile testing. This notch removal process is shown schematically in Fig. 1. After lapping, the planarized surface was lightly bead blasted with 25 μm diameter Al_2O_3 beads to create a roughened surface that provided sufficient optical contrast or "speckling" for image correlation and tracking.

Testing was performed with an MTS 20 kip (90 kN) servohydraulic load frame. A conventional extensometer with a 0.5 in. (12.5 mm) gage section was used in the central region

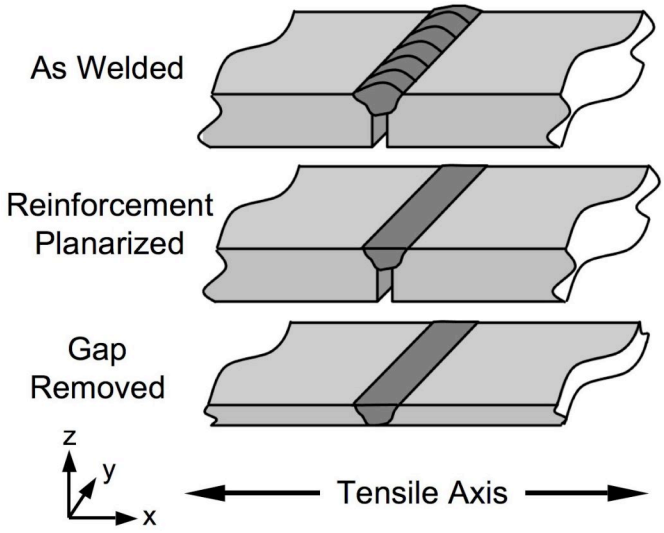

Figure 1: Tensile sample preparation and principal axes orientation.

of the welded tensile bar to compare directly to the DIC strain field analysis. Tensile tests were performed at a constant displacement rate of 0.002 in/s (0.05 mm/s), which corresponded to an apparent strain rate over the 0.5 in. (12.5 mm) gauge length of 7×10^{-4} s^{-1}.

Digital images of the deforming surface were captured once per second using an Allied Vision Technologies Marlin F-145B2 firewire camera with a 1392×1040 pixel CCD. A photographic macro lens was used to project the image of the 0.25 in. (6.35 mm) wide tensile bar onto the 0.5 in. (12.7 mm) CCD. The field of view projected onto the CCD corresponded to a pixel resolution of 8.2×8.2 μm. VicSNAP software from Correlated Solutions, Inc. was used to capture the images along with a corresponding data file containing time, force and extensometer strain data. Vic-2D was used to correlate the resulting images for the calculation of displacement and strain. Image subsets were analyzed on a periodic grid over a region of interest that included almost the entire width of the welded region of ~0.24 in. (6 mm) as well as base metal on either side of the butt weld. In the analysis, each subset was assumed to undergo an affine transformation and a Non-Normalized Correlation (NNC) criterion was used for optimization of the cubic B-spline displacement field [17]. Under the conditions used, strain resolution was estimated to be less than 0.002.

Metallographic cross sections, transverse to the welding direction, were prepared from untested welds and polished using standard metallographic procedures. These cross sections were examined by using light optical microscopy (LOM) as well as electron backscattered electron diffraction (EBSD) in a scanning electron microscope. Microhardness traces were also used to assess the variation in hardness across the weldments. Microhardness tests were conducted by using a Vickers indenter and a 100 gm load.

Results and Discussion

Strain Distributions

Fig. 2 shows typical images and x direction principal strains (ε_{xx}) within a DIC region of interest centered on the CW weld. Images are shown prior to straining, at an intermediate strain level, and at the time of fracture (which occurred well away from the weld in the 304L base metal). The strain contour plots in the deformed state are referenced to the original region of interest. As might be expected, both the images and strain correlations show that strain is almost entirely concentrated in the 304L, and that little or no deformation of the PH 13-8 Mo occurs. The deformation response of the pulsed weld was very similar to that shown in Fig. 2, except that the strain gradients across the weld FZ were somewhat less steep than those in the CW weld.

As shown in Fig. 3, there are a variety of checks that can be applied to assure the validity of the strain correlations. In the example shown, correlation of the Poisson contraction (ε_{yy}) can be verified directly against the macroscopic contraction of the test sample, and in this case the measured contraction of approximately 15% compares well with the DIC correlation at the point shown. Additional checks can be made by using other visible features, though comparison of average strains as measured with the mechanical extensimeter, and through consistency checks provided by the correlation software.

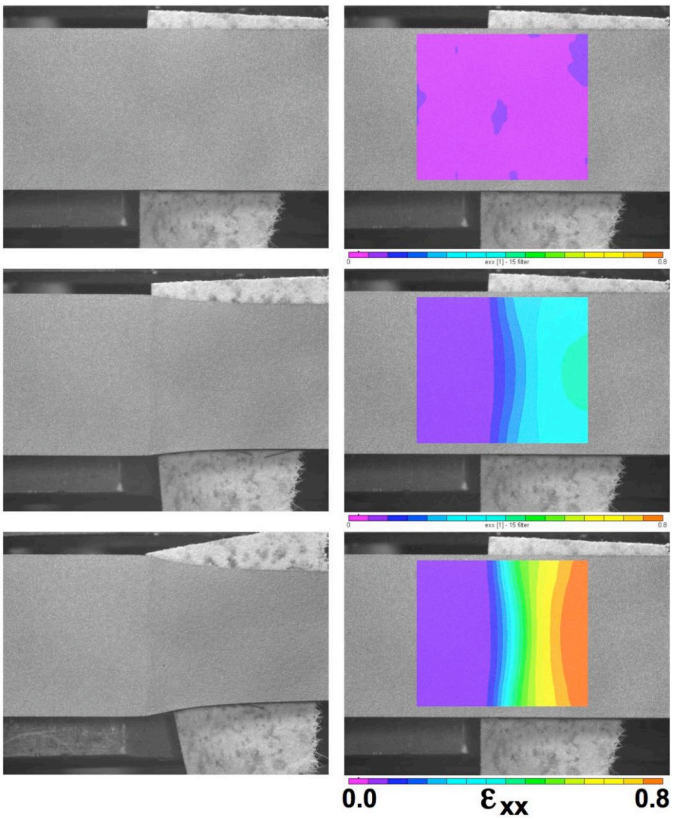

Figure 2: Tensile test images and ε_{xx} from CW laser weld between PH 13-8 Mo (left side) and 304L.

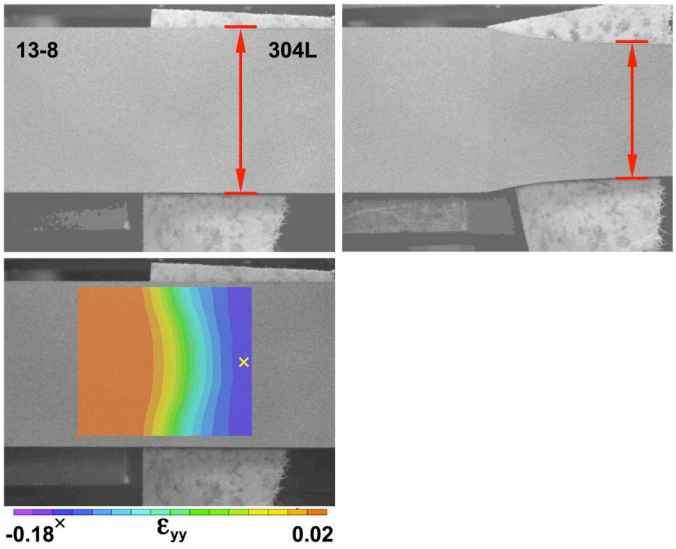

Figure 3. Images and transverse strain contours showing method for validation of strain correlations. DIC ε_{yy} used for comparison taken from point marked x.

Both the longitudinal and transverse strains, ε_{xx} and ε_{yy} in Figs. 2 and 3, show the high level of constraint imposed by the PH 13-8 Mo, and virtually all the plastic deformation occurs within the weld FZ and the 304L. Of course, this is to be expected given the high strength levels of PH 13-8 Mo, in either the H950 or H1100 aged condition, relative to 304L. Within the weld joint, the constraint results in bowing of both the ε_{xx} and ε_{yy} contours along the load centerline of the sample and toward the 304L and consequently a biaxial stress state within the weld FZ.

Stress-Strain Response

Stress-strain curves were extracted from the various regions of the laser welds and this is illustrated in Fig. 4 for the CW weld. Stress-strain curves for the entire strain range as well as in the low strain region of the test are shown. For these constructions, the stress is assumed to be the continuum engineering stress at all locations throughout the test. The stress-strain curves illustrate the ability of the DIC technique to determine strain over a wide range within the weldment; from elastic within the PH 13-8 Mo base metal to over 70% strain within the 304L base metal. Within the weld FZ (point 2 in the image) the 0.2% offset yield strength was observed to be approximately 50 ksi (344 MPa) compared with approximately 45 ksi (310 MPa) for the 304L base metal away from the weld, and this provides an indication of the sensitivity of the DIC technique. These yield strength values are a consequence of both the microstructure of the welds as discussed below and the biaxial stress state within the weld FZ. Conversely, the mechanical extensometer is incapable of discerning these differences, and provides only an average representation of the overall response. Stress-strain curves extracted from the pulsed laser weld were similar to those shown in Fig. 4.

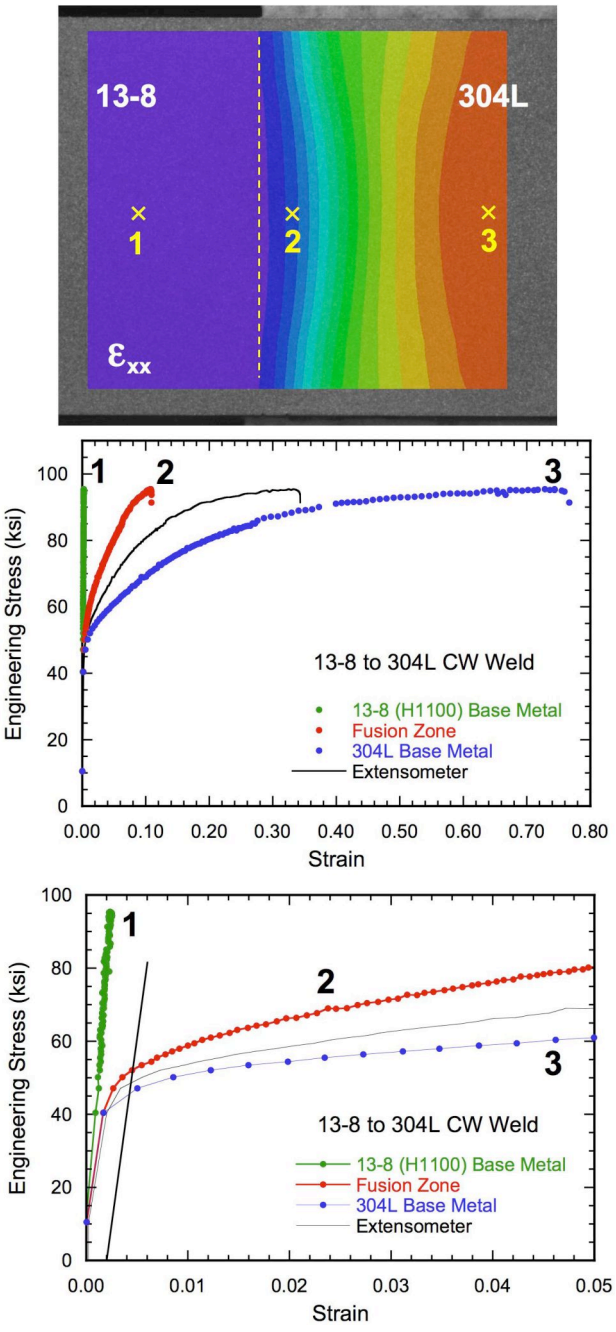

Figure 4: Stress-strain curves extracted from three principal regions of CW laser weld. Dashed line shows location of PH 13-8 Mo/FZ boundary. Also shown is curve extracted from mechanical extensometer data.

Phase and Spectral Image Mapping

Light optical photomicrographs and EBSD analysis of the CW and pulsed welds are shown in Fig. 5. Both weld procedures resulted in predominantly ferritic (or potentially martensitic since EBSD cannot easily distinguish between ferrite and martensite) microstructures, and are relatively fine grained relative to the annealed 304L base metal. The finer grain size and generally ferritic microstructures likely both contribute to

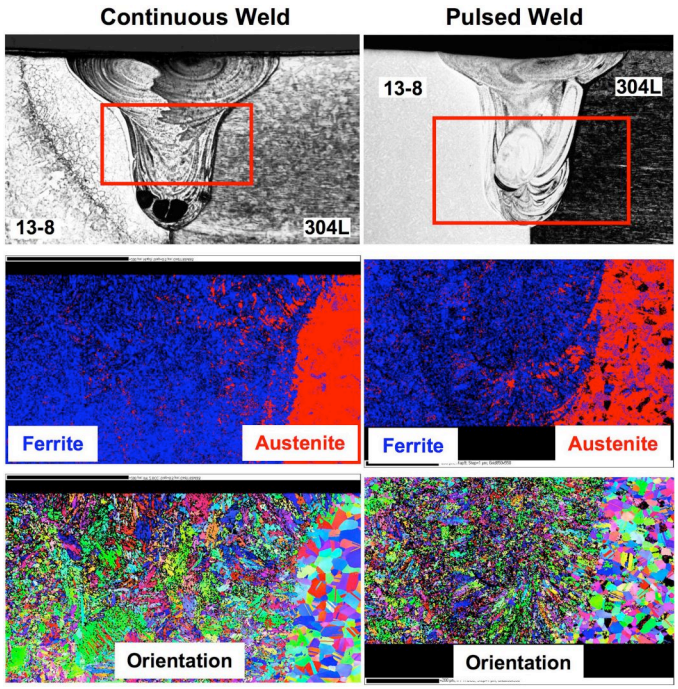

Figure 5: Phase and orientation maps for CW and pulsed PH 13-8 Mo to 304L laser welds. EBSD analysis area shown as a red box in the optial micrographs.

the higher strength (relative to the 304L) observed in the weld FZ. The maps also show that both procedures result in appreciable quantities of residual austenite in the portion of the FZ adjacent to the 304L base metal, and thus there is appreciable structural inhomogeneity within the FZ of the CW and pulsed welding procedures. As might be expected, the microstructures of fusion zone was similar for both H950 and H1100 PH 13-8 Mo heat treatments. No predominant crystallographic texturing is evident in either weld or the two base metals, and is similar to observations made previously [15].

Fig. 6 shows a spectral image of the CW weld in terms of two predominant spectra types. These types are based on spectral components that contain two distinct features, *i.e.* spectra corresponding to PH 13-8 Mo-like regions (containing Fe, Cr, Ni, Mn, and Si along with significant quantities of Mo and Al), and spectra corresponding to 304L-like regions (containing Fe, Cr, Ni, Mn and Si and no Mo or Al). Thus, the blue regions in Fig. 6 are those that compositionallly are predominantly PH 13-8 Mo in character, while the red regions are those that are predominantly 304L in character. From this analysis, the etched LOM image of Fig. 5, and the EBSD results in Fig. 5, is it apparent that mixing in the CW weld is not complete. Similar results were obtained from the pulsed weld, although the mixing pattern was different and somewhat more complete in the pulsed weld due to the multiple remelting cycles inherent in the pulsed procedure. Comparison of the EBSD analysis area of the CW weld in Fig. 5 with the same area in the spectral image of Fig. 6 shows that although

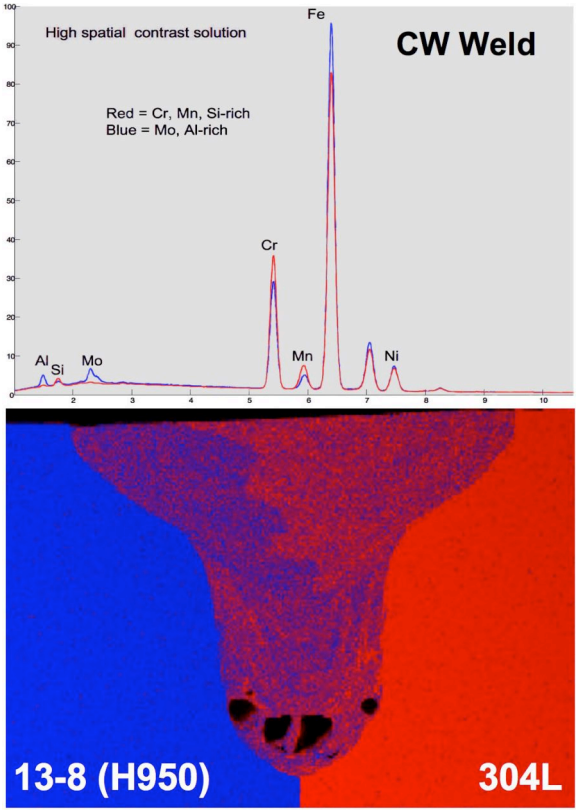

Figure 6. Spectral image of CW PH 13-8 Mo to 304L laser weld.

the right hand side of the spectral image contains appreciable amounts of 304L-like spectra, the region is predominantly ferritic (or martensitic) with only small amounts of retained or residual austenite.

Microhardness

Microhardness traces across the CW and pulsed welds are shown in Fig. 7, and these reveal several interesting differences between the CW and pulsed welds. Considering first the heat-affected zone (HAZ) in the PH 13-8 Mo side of the weld, it is apparent that the softened region in the HAZ (presumably due to reaustenitization and/or overaging) is appreciably wider in the CW weld. This region extends approximately 500 μm in the CW weld versus approximately 300 μm in the pulsed weld. The difference is a result of the short pulse length and steep thermal gradients associated with the pulsed procedure used.

With respect to the fusion zone, the pulsed weld shows uniform hardness across the location examined, and the hardness is similar to the annealed 304L base metal. This implies that the FZ in the pulsed weld is comparatively well mixed and from EBSD is ferritic (not martensitic). The comparatively uniform mixing is due to the remelting of each region during subsequent pulses (75-80% spot overlap) so that each region is remelted several times during welding. Conversely, the CW weld show variable hardness with the PH 13-8 Mo side of the FZ exhibiting hardness approaching that of the PH 13-8 Mo HAZ. This implies that the mixing within the CW weld is less complete than that in the pulsed weld. Further, since the entire FZ in the CW weld was observed to have a predominantly bcc crystal structure, it is likely that the 304L side of the FZ is ferritic while the PH 13-8 Mo side of the FZ is martensitic. It should also be noted that this observation is typical of a number of CW and pulsed weld sections examined, and is not unique to the sections shown in Figs. 5-7.

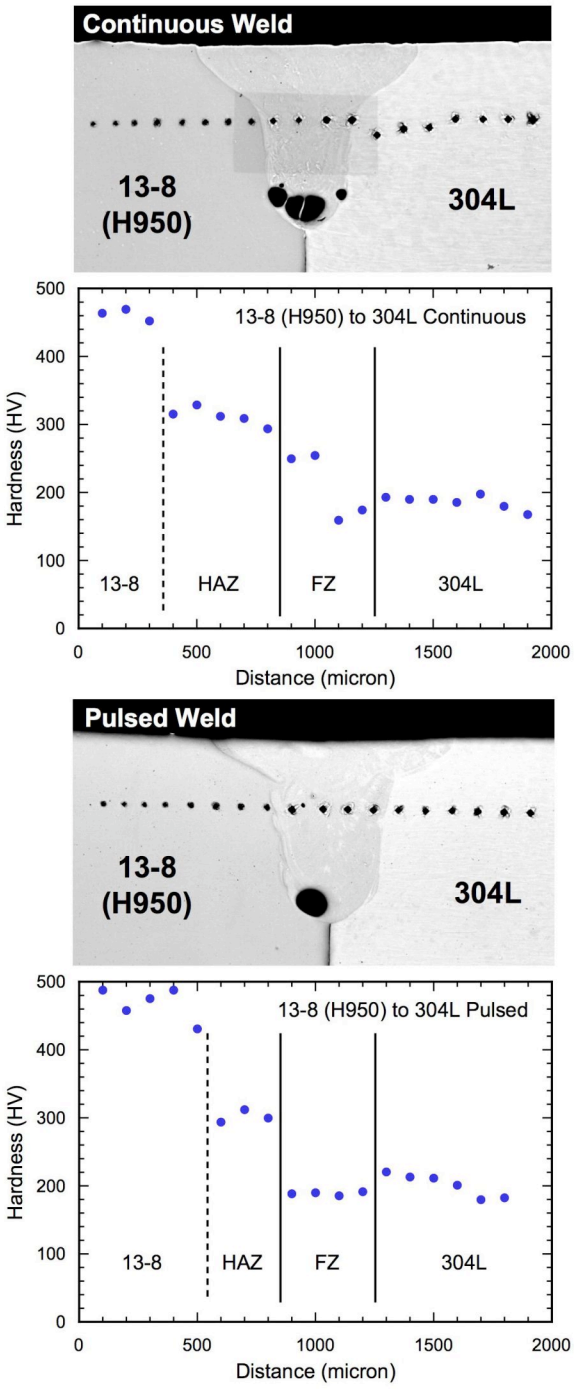

Figure 7. Micrographs and microhardness traces across CW and pulsed laser welds.

Given the differences in HAZ width and FZ microstructure between the CW and pulsed welds, it might be expected that there would be small differences in the mechanical response of the CW versus pulsed welds. At the present time, we have not conducted the DIC analysis at sufficient resolution to clearly detect these small differences between the CW and pulsed welds. However, there is no fundamental reason why these differences cannot be detected by DIC methods. Given the shape of the hardness profiles in Fig. 7, and assuming sufficient image magnification in the DIC data acquisition, the CW weld should display somewhat shallower strain gradients than the pulsed weld and this was qualitatively observed. These detailed differences between the CW and pulsed welds, as well as the behavior of other strain components (*e.g.* ε_{yy}, ε_{xy}) and DIC observations from the side of the test sample will be discussed in more detail in a future article.

It should noted that, as implemented here, the DIC method can only observe strain on the surface of the test sample. While the general principles can be extended to 3D image correlation, the 2D method requires only a single image plane under the assumption that little or no deformation occurs out of plane. This assumption is acceptable in the case of planar tensile bars with negligible triaxial necking such as those used here. In addition, out of plane motions, as might be expected from differences in properties in the though thickness direction can contribute to uncertainty. For the tests described here, appreciable out of plane motion (bending) was not observed. However, due to the shape of the welds evaluated here, a through thickness gradient in the weld width in the loading direction cannot be avoided even for relatively thin test samples, so there is likely some asymmetry in the deformation through thickness. Finally, the nature of the dissimilar welds here is interesting in that the PH 13-8 Mo side of the joint remains essentially elastic during the entire test. As a result, the material in the vicinity of the PH 13-8 Mo fusion line is severely constrained and effectively experiences a biaxial loading conditions.

Thus, altthough additional refinements of the DIC method and analysis are desirable and are planned for future work, it is clear that the DIC method provides a means to determine properties under situations that were previously inaccessible. This and previous work on laser welds [15, 16] indicate that both weld size and strength gradients within the weld do not restrict the ability of the technique to extract important and useful mechanical properties information.

Conclusions

The digital image correlation technique for localized strain mapping has been successfully applied to small laser welds and can detect and quantify the strain gradients in welds with large strength and ductility differences across the joint. From the DIC strain determinations, local stress-strain response can be inferred for the various weld regions of interest, and these constitutive properties are useful for assessing weld performance, mechanical modeling, and for verifying analytical predictions.

For the dissimilar welds examined, mixing in the CW weld appeared to be less complete than in the pulsed weld, and the CW weld likely contained both martensitic and ferritic regions as well as austenite, while the pulsed weld appeared to be predominantly ferritic with some residual austenite. Yield strength for both welds was generally consistent with ferritic steels, although biaxial constraint probably also contributed to the observed yield behavior. Although the differences in microstructure between the CW and pulsed welds are relatively small, it is expected that additional refinement of DIC resolution and analysis technique will be capable of detecting these differences.

Acknowledgements

Sandia is a multiprogram laboratory operated by Sandia Corporation, a Lockheed Martin Company, for the United States Department of Energy's National Nuclear Security Administration under contract DE-AC04-94AL85000. The authors would like to thank J. R. Michael for the EBSD analysis, P. G. Kotula for the spectral imaging, D. L. La Pierre for the microhardness testing, and J. D. Puskar for review of the manuscript.

References

1. Y. Cui and C.D. Lundin, "Effect of microfissures on mechanical properties of 308L austenitic stainless steel weld metals", *Journal of Materials Science*, vol. 40, p. 1281-1283, 2005.
2. J.R. Foulds, J. Moteff, V.K. Sikka, and J.W. McEnerney, "Deformation behavior of a 16-8-2 GTA weld as influenced by its solidification substructure", *Metallurgical Transactions A*, vol. 14A, p. 1357-1366, 1983.
3. J.A. Brooks, S.H. Goods, and C.V. Robino, "Weld properties of a free machining stainless steel", Sandia National Laboratories Report SAND2000-8002, August, 2000.
4. W. Tong, H. Tao, X. Jiang, N. Zhang, M.P. Marya, L.G. Hector, Jr., and X.Q. Gayden, "Deformation and fracture of miniature tensile bars with resistance-spot-weld microstructures", *Metallurgical and Materials Transactions A*, vol. 36A, p. 2651-2669, 2005.
5. S.M. Zuniga and S.D. Sheppard, "Determining the constitutive properties of the heat-affected zone in a resistance spot weld", *Modeling and Simulation in Materials Science and Engineering*, vol. 3, p. 391-416, 1995.
6. J.F. Zarzour, P.J. Konkol, and H. Dong, "Stress-strain characteristics of the heat-affected zone in an HY-100 weldment as determined by microindentation testing", *Materials Characterization*, vol. 37, p. 195-209, 1996.

7. E. Markiewicz, P. Ducrocq, P. Drazetic, G. Haugou T. Fourmentraux, and J.Y. Berard, "Material behaviour law identification for the various zones of the spot-weld under quasi-static loadings", *International Journal of Materials and Product Technology*, vol. 16, p. 484-509, 2001.
8. M.J. McGinnis, S. Pessiki, and H. Turker, "Application of three-dimensional digital image correlation to the core-drilling method", *Experimental Mechanics*, vol. 45, p. 359-67, 2005.
9. J. Kang , D.S. Wilkinson, M. Jain, J.D. Embury, A.J. Beaudoin, S. Kim, R. Mishira, and A.K. Sachdev, "On the sequence of inhomogeneous deformation processes occurring during tensile deformation of strip cast AA5754", *Acta Materialia,* vol. 54, p. 209–218, 2006.
10. A.P. Reynolds and F. Duvall, "Digital image correlation for determination of weld and base metal constitutive behavior" *Welding Journal*, vol. 78, p.355S-360S, 1999.
11. W.D. Lockwood, B. Tomaz, and A.P. Reynolds, "Mechanical Response of friction stir welded AA2024: experiment and modeling", *Materials Science and Engineering A*, vol. A323, p. 348-353, 2002.
12. W.D. Lockwood and A.P. Reynolds, "Simulation of the global response of a friction stir weld using local constitutive behavior", *Materials Science and Engineering A*, vol. A339, p. 35-42, 2003.
13. C. Genevois, A Deschamps, A. Denquin, B. Doisneau-cottignies, "Quantitative investigation of precipitation and mechanical behaviour for AA2024 friction stir welds", *Acta Materialia*, vol 53, p. 2447-2458, 2005.
14. C. Genevois, A. Deschamps, and P. Vacher, "Comparative study on local and global mechanical properties of 2024 T351, 2024 T6, and 5251 O friction stir welds", *Materials Science and Engineering A*, vol. 415, p. 162-170, 2006.
15. B.L Boyce, P.L Reu, and C.V. Robino, The Constitutive Behavior of Laser Welds in 304L Stainless Steel Determined by Digital Image Correlation, *Metallurgical and Materials Transactions A*, Volume 37A, Number 8, August 2006, pp. 2481-2492.
16. W. Tong, L.G. Hector, Jr., C. Dasch, H. Tao, and X. Jiang, Local Plastic Deformation and Failure Behavior of Nd:YAG Laser Welds in AA5182-O and AA6111-T4, *Metallurgical and Materials Transactions A*, Volume 38A, Number 12, December 2007, pp. 3063-3086.
17. P. Cheng, M.A. Sutton, H.W. Schreier, and S.R. McNeill, "Full-field Speckle Pattern Image Correlation with B-Spline Deformation Function", *Experimental Mechanics*, 42, p. 344-352, 2002.